



Hierarchical heterostructures of Bi_2MoO_6 microflowers decorated with Ag_2CO_3 nanoparticles for efficient visible-light-driven photocatalytic removal of toxic pollutants

Shijie Li^{*1}, Wei Jiang¹, Shiwei Hu¹, Yu Liu¹, Yanping Liu², Kaibing Xu^{*3} and Jianshe Liu⁴

Full Research Paper

[Open Access](#)

Address:

¹Key Laboratory of Key Technical Factors in Zhejiang Seafood Health Hazards Institute of Innovation & Application, Zhejiang Ocean University, Zhoushan, Zhejiang Province 316022, China, ²Department of Environmental Engineering, Zhejiang Ocean University, Zhoushan, Zhejiang Province 316022, China, ³State Key Laboratory for Modification of Chemical Fibers and Polymer Materials, Research Center for Analysis and Measurement, Donghua University, Shanghai 201620, China and ⁴State Environmental Protection Engineering Center for Pollution Treatment and Control in Textile Industry, College of Environmental Science and Engineering, Donghua University, Shanghai 201620, China

Email:

Shijie Li^{*} - lishijie@zjou.edu.cn; Kaibing Xu^{*} - xukaibing@dhu.edu.cn

^{*} Corresponding author

Keywords:

antibiotic removal; Bi_2MoO_6 ; heterojunction; silver carbonate (Ag_2CO_3)

Beilstein J. Nanotechnol. **2018**, *9*, 2297–2305.

doi:10.3762/bjnano.9.214

Received: 11 May 2018

Accepted: 13 August 2018

Published: 27 August 2018

Associate Editor: J. J. Schneider

© 2018 Li et al.; licensee Beilstein-Institut.

License and terms: see end of document.

Abstract

Developing highly active and durable visible-light-driven photocatalysts for the degradation of toxic pollutants is of vital significance. Herein, Ag_2CO_3 nanoparticles were in situ formed on Bi_2MoO_6 microflowers to produce $\text{Ag}_2\text{CO}_3/\text{Bi}_2\text{MoO}_6$ heterostructures via a facile procedure. The morphologies, phases, chemical compositions, and optical properties of $\text{Ag}_2\text{CO}_3/\text{Bi}_2\text{MoO}_6$ were examined by multiple characterization techniques. The $\text{Ag}_2\text{CO}_3/\text{Bi}_2\text{MoO}_6$ heterostructures exhibited substantially improved performance in the removal of industrial dyes (rhodamine B (RhB), methyl orange (MO), and methyl blue (MB)), and the antibiotic tetracycline hydrochloride (TC), compared with bare Bi_2MoO_6 and Ag_2CO_3 under visible-light irradiation. The enhancement of activity was attributed to the high charge-separation capacity, which results from the matched band alignment of the two components. The cycling experiments showed a good durability of $\text{Ag}_2\text{CO}_3/\text{Bi}_2\text{MoO}_6$. Holes were found to be the dominant active species accounting for the pollutant degradation. This compound is a promising candidate for wastewater treatment.

Introduction

Industrial pollutants, such as industrial dyes and antibiotics, in wastewaters pose a huge threat to the environment [1,2]. Thus, many methods for pollutant removal have been established. However, the conventional wastewater treatments are usually accompanied by high cost, low efficiency and other insufficiencies [2]. The decomposition and mineralization of pollutants under sunlight through photocatalysis has been demonstrated to be an effective and green technology for environmental remediation [3–6]. Crucial to photocatalysis is to obtain high-performance photocatalysts [7,8]. Obtaining excellent photocatalysts that can be excited by visible light (43% of the solar energy spectrum) is very important for practical applications [9–14].

Bi_2MoO_6 has been regarded as a promising visible-light-driven (VLD) photocatalyst because of its good activity, chemical stability and nontoxicity [15–17]. However, the low carrier-separation rate and narrow photo-response range of Bi_2MoO_6 substantially lower its photocatalytic performance [18,19]. To overcome this obstacle, various methods have been developed, including doping [20,21] and the construction of heterojunctions [22–33]. Particularly, the combination of Bi_2MoO_6 with other semiconductors to construct heterojunction photocatalysts leads to an enhanced activity of Bi_2MoO_6 , which originates from the increased charge separation at the interface [22–30].

Recently, Ag-based compounds (e.g., Ag_3PO_4 , Ag_3VO_4 , Ag_2CrO_4 , and Ag_2CO_3) [34–36] have emerged as good VLD photocatalysts for pollutant removal. Ag_2CO_3 exhibits a high visible-light photocatalytic activity [37]. However, it is unstable under illumination. Previous studies found that the good stability of Ag_2CO_3 could be achieved through the rational construction of heterojunctions, such as $\text{Ag}_2\text{CO}_3/\text{Bi}_2\text{WO}_6$ [37], $\text{Ag}_2\text{O}/\text{Ag}_2\text{CO}_3$ [38], $\text{Ag}_2\text{CO}_3/\text{Bi}_2\text{O}_2\text{CO}_3$ [39], $\text{Ag}_2\text{CO}_3/\text{C}_3\text{N}_4$ [40], $\text{Ag}/\text{Ag}_2\text{CO}_3/\text{BiVO}_4$ [41], $\text{Ag}_2\text{CO}_3/\text{AgBr}/\text{ZnO}$ [42], and $\text{Ag}/\text{Ag}_2\text{CO}_3/\text{Bi}_2\text{MoO}_6$ [32]. The band structure of Ag_2CO_3 matches well with that of Bi_2MoO_6 [32]. Moreover, morphology modulation is another significant way to enhance photocatalytic activity. Three-dimensional nanostructures endow materials with unique physicochemical properties, for instance, high specific surface area, good molecular diffusion/transport, and good recyclability and light harvesting ability. To the best of our knowledge, application of Ag_2CO_3 nanoparticles coupled with flower-like Bi_2MoO_6 for photocatalytic degradation of toxic pollutants remains unreported.

Herein, we synthesized flower-like $\text{Ag}_2\text{CO}_3/\text{Bi}_2\text{MoO}_6$ heterostructures, in which Ag_2CO_3 nanoparticles were evenly anchored on Bi_2MoO_6 microflowers to construct novel hierarchical heterojunction photocatalysts by via in situ precipitation. The photocatalytic properties of $\text{Ag}_2\text{CO}_3/\text{Bi}_2\text{MoO}_6$ was

measured regarding the photocatalytic degradation of industrial dyes (rhodamine B (RhB), methyl orange (MO), and methyl blue (MB)), and the antibiotic tetracycline hydrochloride (TC) under visible light. The improved performance of the photocatalytic degradation was prominent, and the reasons were rationally analyzed. Also, the photocatalytic mechanism of pollutant degradation over $\text{Ag}_2\text{CO}_3/\text{Bi}_2\text{MoO}_6$ was discussed.

Results and Discussion

Characterization of catalysts

A series of flowerlike $\text{Ag}_2\text{CO}_3/\text{Bi}_2\text{MoO}_6$ heterostructures with different weight ratios (0.1/1, 0.2/1, 0.3/1, and 0.5/1) were constructed and labeled ACO/BMO-10, ACO/BMO-20, ACO/BMO-30, and ACO/BMO-50, respectively. The crystal structure of Bi_2MoO_6 , Ag_2CO_3 , and $\text{Ag}_2\text{CO}_3/\text{Bi}_2\text{MoO}_6$ heterostructures were determined by XRD technique (Figure 1). The diffraction peaks of Ag_2CO_3 and Bi_2MoO_6 were indexed as orthorhombic Bi_2MoO_6 (JCPDS 76-2388) and monoclinic Ag_2CO_3 (JCPDS 26-0399), respectively. The XRD pattern of these heterostructures show the characteristic peaks of both Ag_2CO_3 and Bi_2MoO_6 , indicating the successful synthesis of $\text{Ag}_2\text{CO}_3/\text{Bi}_2\text{MoO}_6$ heterostructures. In another publication, $\text{Ag}/\text{Ag}_2\text{CO}_3/\text{Bi}_2\text{MoO}_6$ nanoplates, composed of three phases, have been described [32].

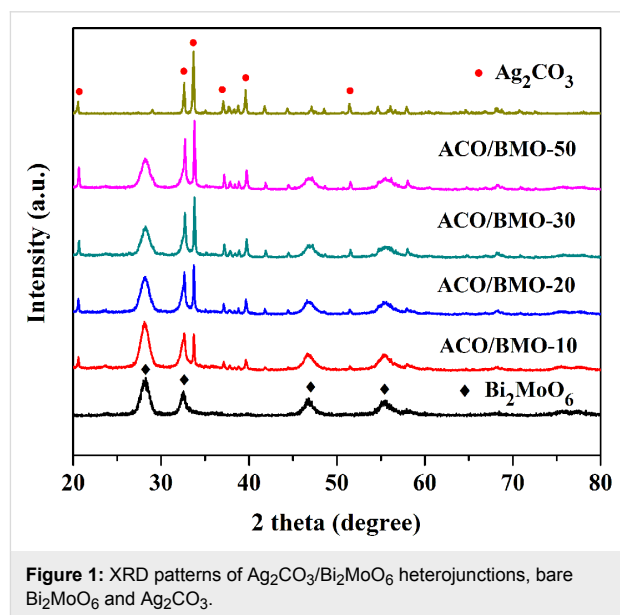


Figure 1: XRD patterns of $\text{Ag}_2\text{CO}_3/\text{Bi}_2\text{MoO}_6$ heterojunctions, bare Bi_2MoO_6 and Ag_2CO_3 .

To visually study the microstructure and morphology of $\text{Ag}_2\text{CO}_3/\text{Bi}_2\text{MoO}_6$, SEM images of the as-prepared catalysts were taken. Bare Bi_2MoO_6 presents a hierarchical microsphere structure (diameter: 1.6–3.5 μm , Figure 2a,b). After Ag_2CO_3 was loaded onto Bi_2MoO_6 , the resulting $\text{Ag}_2\text{CO}_3/\text{Bi}_2\text{MoO}_6$ retained the flower-like architecture. The representative

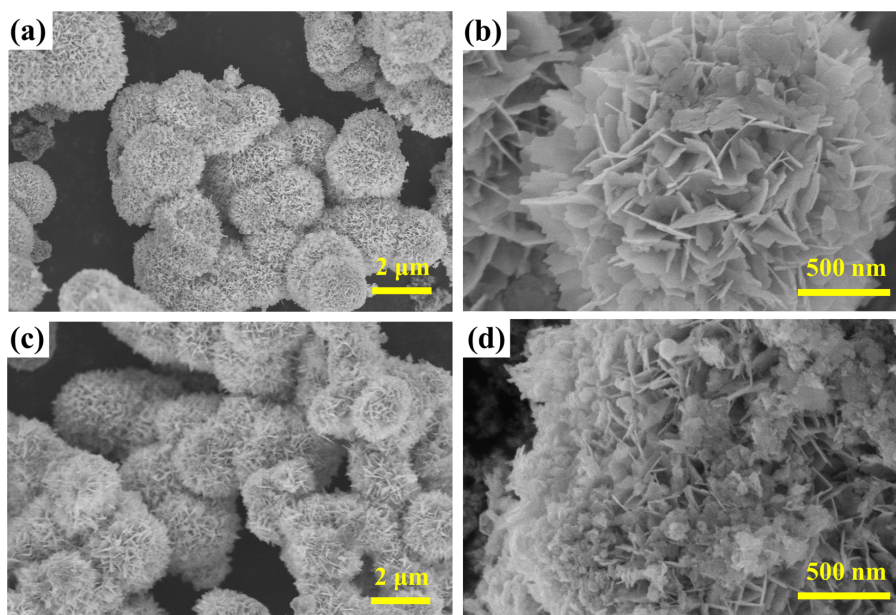


Figure 2: SEM images of (a, b) bare Bi_2MoO_6 and (c, d) ACO/BMO-30.

ACO/BMO-30 displays the flower-like structure, the surface of which is decorated with Ag_2CO_3 nanoparticles (size: 10–50 nm, Figure 2c,d). In contrast, the previously reported $\text{Ag}/\text{Ag}_2\text{CO}_3/\text{Bi}_2\text{MoO}_6$ is composed of Bi_2MoO_6 nanoplates and $\text{Ag}/\text{Ag}_2\text{CO}_3$ nanorods/nanoparticles [32].

Further information about the structure of ACO/BMO-30 was collected from TEM images (Figure 3). The TEM images are in line with the SEM observations, i.e., ACO/BMO-30 exhibits a flower-like architecture loaded with Ag_2CO_3 nanoparticles (Figure 3a,b). The HRTEM displays two different lattice spac-

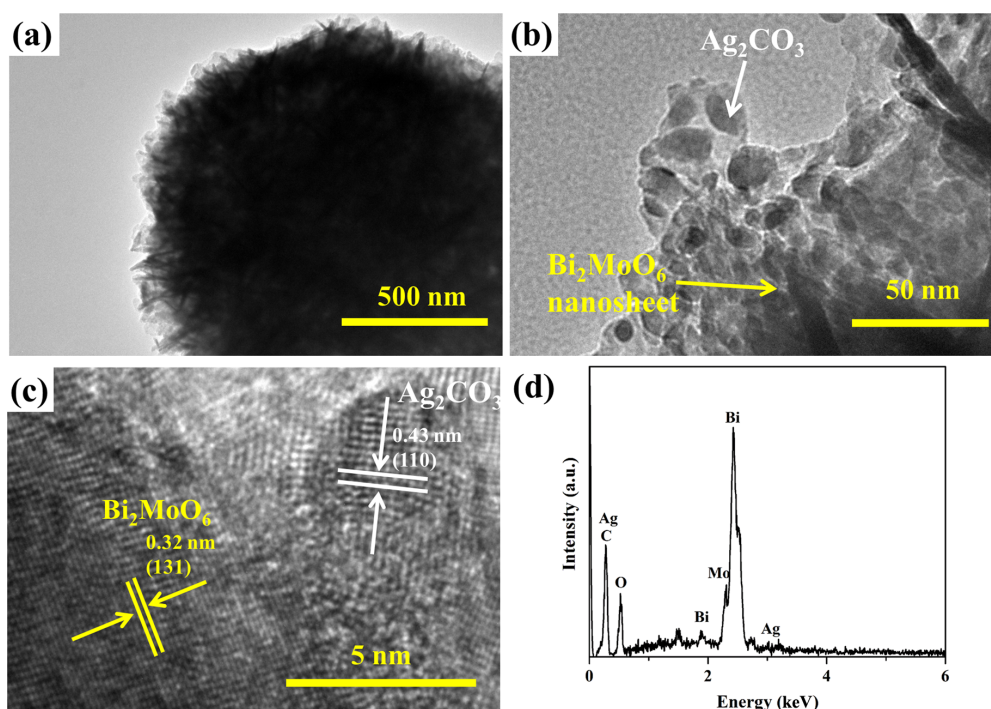


Figure 3: (a–c) TEM images of ACO/BMO-30; (d) EDS pattern of ACO/BMO-30.

ings of 0.32 and 0.43 nm, which match well with the (121) planes of orthorhombic Bi_2MoO_6 and the (110) planes of monoclinic Ag_2CO_3 (Figure 3c). Moreover, the energy-dispersive spectroscopy (EDS) pattern confirmed the existence of Ag, C, O, Bi, and Mo in ACO/BMO-30 (Figure 3d).

The optical absorption of Bi_2MoO_6 , Ag_2CO_3 and $\text{Ag}_2\text{CO}_3/\text{Bi}_2\text{MoO}_6$ heterostructures were measured by using UV–vis diffuse reflection spectra (UV–vis DRS, Figure 4). The absorption edges of Ag_2CO_3 and Bi_2MoO_6 are around 570 nm and 470 nm, respectively, in line with already reported values [30,33,39]. Compared to pristine Bi_2MoO_6 , the absorption of the $\text{Ag}_2\text{CO}_3/\text{Bi}_2\text{MoO}_6$ heterostructures was substantially improved owing through the introduction of Ag_2CO_3 nanoparticles. $\text{Ag}/\text{Ag}_2\text{CO}_3/\text{Bi}_2\text{MoO}_6$ [32], $\text{Ag}_2\text{MoO}_4/\text{Bi}_2\text{MoO}_6$ [22], and $\text{Ag}_2\text{CO}_3/\text{Bi}_2\text{MoO}_6$ heterostructures are VLD photocatalysts.

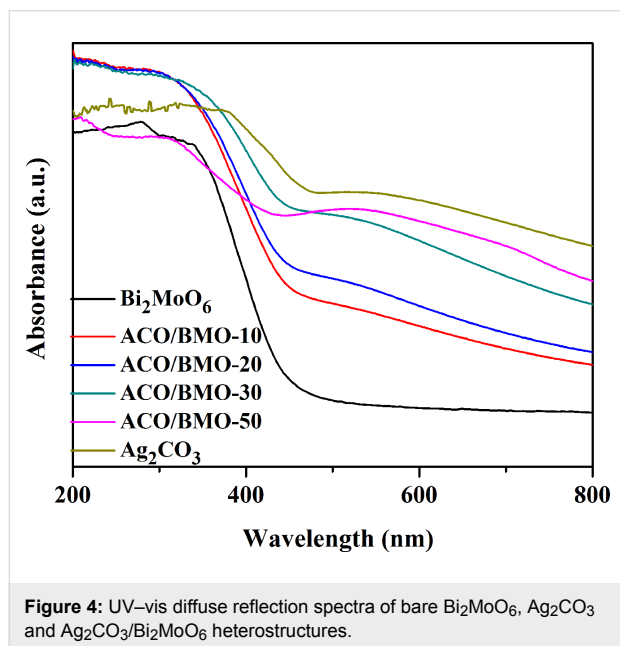


Figure 4: UV–vis diffuse reflection spectra of bare Bi_2MoO_6 , Ag_2CO_3 and $\text{Ag}_2\text{CO}_3/\text{Bi}_2\text{MoO}_6$ heterostructures.

The band gap energy (E_g) can be estimated from the Tauc plot: $(\alpha h\nu) = A(h\nu - E_g)^{n/2}$. Where α , h , ν , and A are absorption coefficient, Planck's constant, the frequency of light, and a constant, respectively. The value of n depends on the type of electronic transition and n is equal to 1 for Bi_2MoO_6 and Ag_2CO_3 . The Tauc plots of Ag_2CO_3 and Bi_2MoO_6 converted from the UV–vis DRS measurements are shown in Figure S1 (Supporting Information File 1). The band gaps are determined to be 2.17 for Ag_2CO_3 and 2.66 eV for Bi_2MoO_6 .

The band potentials of Ag_2CO_3 and Bi_2MoO_6 can be estimated by the empirical equations:

$$E_{\text{VB}} = X - E_0 + 0.5E_g, \quad (1)$$

$$E_{\text{CB}} = E_{\text{VB}} - E_g, \quad (2)$$

where the X value for Bi_2MoO_6 is 5.5 eV [43], and that for Ag_2CO_3 is 6.02 eV [44]. The value of E_0 is ca. 4.5 eV. Hence, the values of E_{VB} and E_{CB} of Bi_2MoO_6 were calculated as -0.32 and 2.34 eV, and those of Ag_2CO_3 were calculated as 0.43 and 2.60 eV.

PL spectra were measured to analyze the electron–hole-separation efficiency [45–47]. Figure 5 shows the contrast between the PL spectra of bare Bi_2MoO_6 and of ACO/BMO-30. The emission peak of Bi_2MoO_6 is centered at ca. 465 nm under an excitation wavelength of 300 nm. Intriguingly, the PL emission intensity of Bi_2MoO_6 was reduced after the introduction of Ag_2CO_3 . A similar phenomenon was also found in $\text{Ag}/\text{Ag}_2\text{CO}_3/\text{Bi}_2\text{MoO}_6$ [32] and $\text{Ag}_2\text{MoO}_4/\text{Bi}_2\text{MoO}_6$ [22]. This result shows that the charge separation efficiency is enhanced in ACO/BMO-30.

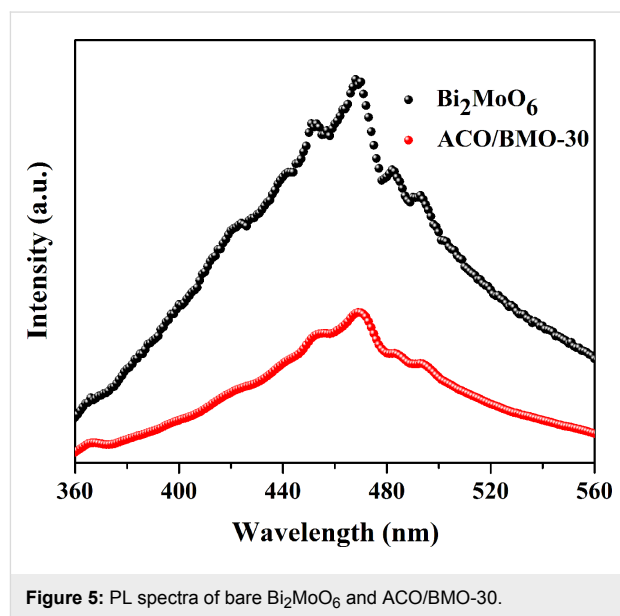
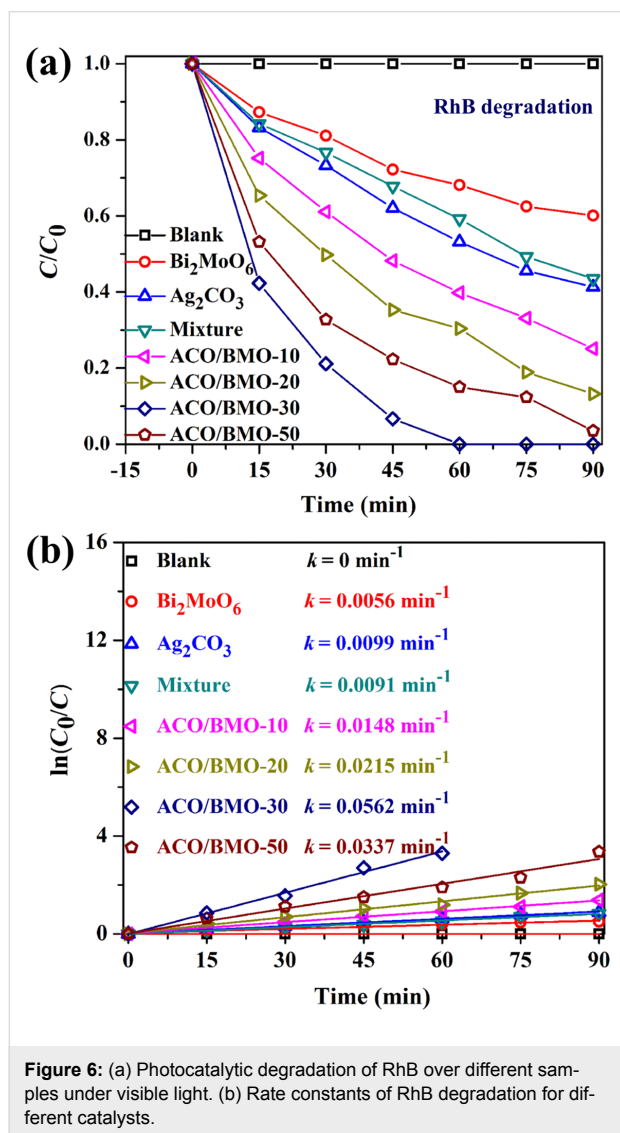


Figure 5: PL spectra of bare Bi_2MoO_6 and ACO/BMO-30.

Photocatalytic performance

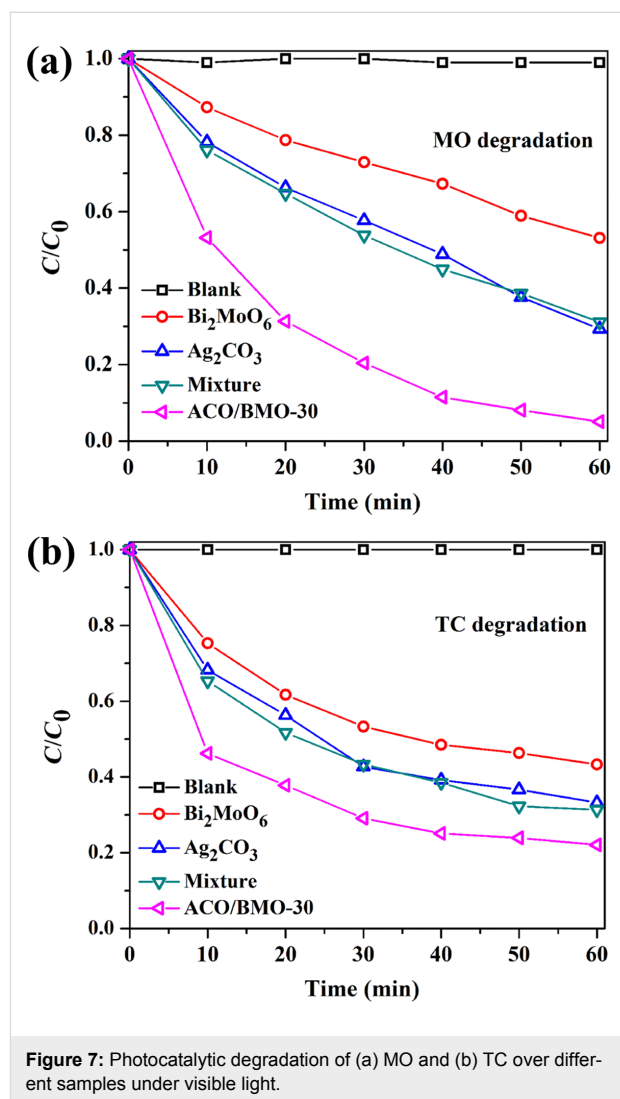
The efficiency of $\text{Ag}_2\text{CO}_3/\text{Bi}_2\text{MoO}_6$ heterostructures in the photocatalytic degradation of industrial dyes (RhB, MO and MB), and the antibiotic TC of the under visible light was measured. Figure 6a displays the degradation of RhB as a function of the time. The RhB concentration remains unchanged in the absence of catalysts. In the presence of bare Bi_2MoO_6 and Ag_2CO_3 only 39.8% and 58.7% of RhB were degraded after 90 min of reaction time. The degradation of RhB was substantially enhanced when a combination of Bi_2MoO_6 and Ag_2CO_3 was used. For instance, the introduction of a low amount of Ag_2CO_3 (10 wt %) resulted in 74.9% degradation of RhB. Obviously, the RhB degradation performance is closely related

to the loading amount of Ag_2CO_3 . Among the heterostructures, ACO/BMO-30 achieves the best activity in the degradation of RhB, with 100% degradation efficiency after 60 min of reaction time. ACO/BMO-10, ACO/BMO-20 and ACO/BMO-50 showed degradation efficiencies of 60.2%, 69.6%, and 85.1%, respectively. Remarkably, a mixture of 23.1 wt % Ag_2CO_3 and 76.9 wt % Bi_2MoO_6 exhibited a much lower activity than ACO/BMO-30, verifying that the close contact between the components also has a significant influence on the photocatalytic performance of the heterostructures.



The pseudo-first-order kinetic plots and rate constants of RhB degradation for various catalysts are presented in Figure 6b. The degradation rate constant of ACO/BMO-30 is 0.0562 min^{-1} , which is 9.0-, 4.7- and 5.2-fold higher than that of bare Bi_2MoO_6 (0.0056 min^{-1}), Ag_2CO_3 (0.0099 min^{-1}), and the mixture (0.0091 min^{-1}).

Figure 7 and Figure S2 (Supporting Information File 1) show the degradation of MO and TC as a function of the time. Again, ACO/BMO-30 displayed the highest activity, with degradation efficiencies of 94.9% for MO, 100% for MB, and 78.9% for TC. The photocatalytic activity in the degradation of TC of ACO/BMO-30 was further compared with that of $\text{Ag}/\text{Ag}_2\text{CO}_3/\text{Bi}_2\text{MoO}_6$ [32], and of $\text{Ag}_2\text{MoO}_4/\text{Bi}_2\text{MoO}_6$ [22]. As shown in Figure S3 (Supporting Information File 1), ACO/BMO-30 is much more active than $\text{Ag}_2\text{MoO}_4/\text{Bi}_2\text{MoO}_6$, but not as active as $\text{Ag}/\text{Ag}_2\text{CO}_3/\text{Bi}_2\text{MoO}_6$ due to the fact that $\text{Ag}/\text{Ag}_2\text{CO}_3/\text{Bi}_2\text{MoO}_6$ is a ternary composite.



To examine the mineralization ability of ACO/BMO-30, the total organic carbon (TOC) was measured during the RhB degradation, and the result is presented in Figure S4 (Supporting Information File 1). Apparently, the TOC removal efficiency gradually goes up with the increase of reaction time and the final TOC removal efficiency is as high as 80.6% after 5 h of

reaction. Hence, ACO/BMO-30 shows a decent mineralization ability.

To test the durability of ACO/BMO-30, repeated runs were carried out under unchanging conditions. As depicted in Figure 8a, after six consecutive runs, the RhB degradation efficiency is still about 92.2%. Additionally, no apparent change of the crystalline structure was found after the photocatalytic reactions, as shown in the XRD pattern (Figure 8b). However, the XPS pattern of the used ACO/BMO-30 suggests that some Ag^+ is reduced to $\text{Ag}(0)$ after the reaction (Figure S5, Supporting Information File 1). It has been recognized that the formation of $\text{Ag}/\text{Ag}_2\text{CO}_3$ shows a stable structure [32]. These results verify that ACO/BMO-30 is stable. It is rationally speculated that ACO/BMO-30 has great potential for the elimination of toxic pollutants.

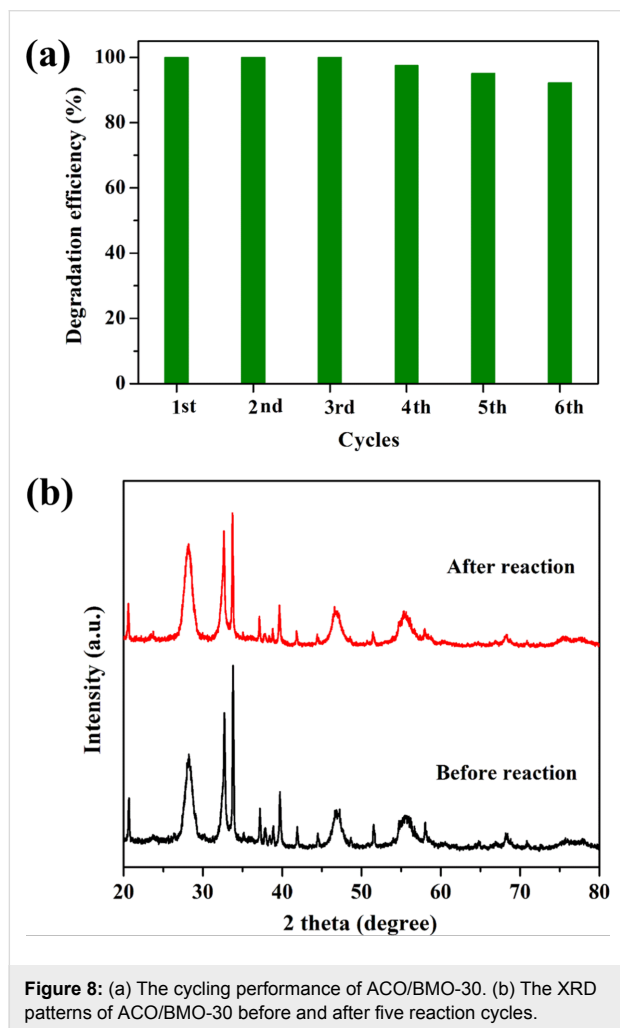
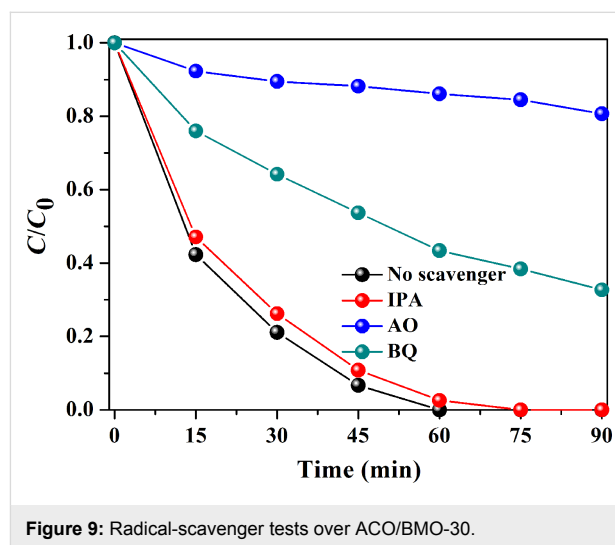


Figure 8: (a) The cycling performance of ACO/BMO-30. (b) The XRD patterns of ACO/BMO-30 before and after five reaction cycles.

Photocatalytic mechanism

In general, radicals and other active species (e.g., $\cdot\text{O}_2^-$, $\cdot\text{OH}$ and h^+) produced in the photocatalytic reaction system contrib-

ute to the decomposition of pollutant [48–52]. We performed radical-scavenger tests to determine the active species in the degradation of RhB. As displayed in Figure 9, the addition of isopropanol (IPA) resulted in a slight inhibition of the RhB degradation, signifying that $\cdot\text{OH}$ is not the major active species. The addition of *p*-benzoquinone (BQ) makes the RhB degradation efficiency decline from 100% to 67.3%, suggesting that $\cdot\text{O}_2^-$ plays a minor role. After the addition of ammonium oxalate (AO) the RhB degradation efficiency decreased from 100% to 19.3%, indicating that h^+ plays a dominant role in the degradation of RhB over $\text{Ag}_2\text{CO}_3/\text{Bi}_2\text{MoO}_6$.



Based on the above results, a possible schematic mechanism is presented in Figure 10. In the $\text{Ag}_2\text{MoO}_4/\text{Bi}_2\text{MoO}_6$ system [22], electron–hole pairs can only be generated by visible light in Bi_2MoO_6 . In comparison, both Ag_2CO_3 and Bi_2MoO_6 are able to absorb visible light and, and charge carriers are photo-generated on the surface of Ag_2CO_3 and Bi_2MoO_6 . The electrons in the CB of Bi_2MoO_6 can partially transfer into that of Ag_2CO_3 . The electrons are then captured by the oxygen, producing $\cdot\text{O}_2^-$ radicals, which play a minor role in decomposing pollutants, as confirmed by the radical-scavenger test (Figure 9). At the same time, the holes in the VB of Ag_2CO_3 can partially flow into that of Bi_2MoO_6 . The holes in both components mainly account for the pollutant degradation (Figure 9). Electron–hole recombination is severely inhibited, as verified by PL results (Figure 5) [53,54]. Although the VB potential of Ag_2CO_3 (2.6 eV) is more positive than that of $\text{H}_2\text{O}/\cdot\text{OH}$ (2.38 eV/NHE at pH 7), the generated $\cdot\text{OH}$ radicals did not act as the major active species for pollutant degradation (Figure 9). In $\text{Ag}/\text{Ag}_2\text{CO}_3/\text{Bi}_2\text{MoO}_6$, $\text{Ag}(0)$ can also be excited to generate electrons, reacting with O_2 to form $\cdot\text{O}_2^-$ radicals due to the plasmon resonance (SPR) effect [32]. Based on above analysis, the rational design and construction of Bi_2MoO_6 -based hetero-

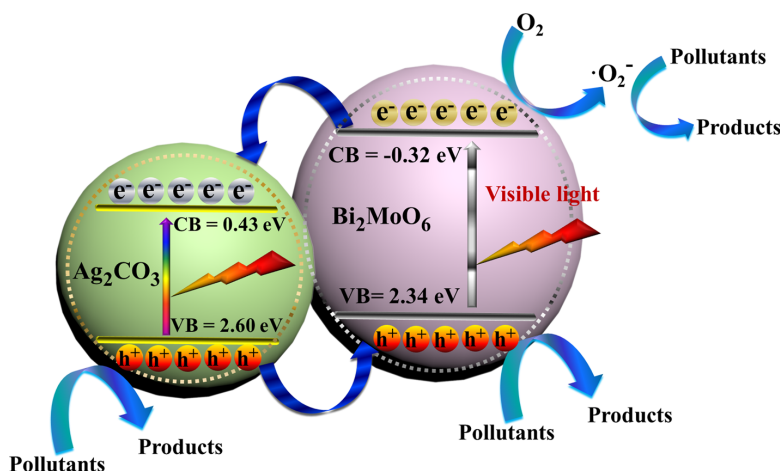


Figure 10: Proposed photocatalytic degradation mechanism of $\text{Ag}_2\text{CO}_3/\text{Bi}_2\text{MoO}_6$.

structures is favorable for the separation of charges, leading to a superior activity in pollutant degradation.

Conclusion

We synthesized a novel photocatalyst of Bi_2MoO_6 micro-flowers covered with Ag_2CO_3 nanoparticles by a facile procedure. The $\text{Ag}_2\text{CO}_3/\text{Bi}_2\text{MoO}_6$ heterostructures, especially ACO/BMO-30, showed a substantially enhanced photocatalytic performance in the removal of pollutants (RhB, MO, MB and TC) under visible light compared to bare Bi_2MoO_6 and Ag_2CO_3 . Moreover, ACO/BMO-30 possesses good durability and stability. The enhanced photocatalytic performance is ascribed to the extended optical response and the matched band structure, reducing carrier recombination. This study offers a novel highly efficient VLD photocatalyst with promising applications in environmental remediation.

Experimental

Materials

$\text{Bi}(\text{NO}_3)_3 \cdot 5\text{H}_2\text{O}$, NaHCO_3 , $\text{NH}_3 \cdot \text{H}_2\text{O}$, $\text{Na}_2\text{MoO}_4 \cdot 2\text{H}_2\text{O}$, rhodamine B (RhB), methyl blue (MB), tetracycline hydrochloride (TC), methyl orange (MO), isopropanol (IPA), AgNO_3 , *p*-benzoquinone (BQ), and ammonium oxalate (AO) were obtained from Chemical Reagent factory (China). All the reagents were used directly without further treatment.

Synthesis

Flower-like Bi_2MoO_6 was synthesized using a solvothermal route. Typically, $\text{Na}_2\text{MoO}_4 \cdot 2\text{H}_2\text{O}$ (1 mmol) was dissolved in a mixture of 40 mL of $\text{CH}_3\text{CH}_2\text{OH}$ and 40 mL of ethylene glycol with the aid of ultrasonic treatment. Then $\text{Bi}(\text{NO}_3)_3 \cdot 5\text{H}_2\text{O}$ (2 mmol) was also dissolved in the above solution in the same way. Subsequently, the solution was magnetically stirred for 1 h, and then loaded into a 100 mL Teflon container and reacted

at 160 °C for 25 h. After the reaction system had cooled down to room temperature, the precipitants were washed thoroughly with deionized water and ethanol, dried, and calcined at 350 °C for 1 h.

$\text{Ag}_2\text{CO}_3/\text{Bi}_2\text{MoO}_6$ heterostructures were obtained by wet-chemical deposition. Typically, 0.6 g Bi_2MoO_6 was ultrasonically dispersed in 30 mL of deionized water. Then AgNO_3 solution (0.1 M) was poured into the suspension and kept stirring for 1 h in the dark. Subsequently, $\text{NH}_3 \cdot \text{H}_2\text{O}$ (0.05 M) was added into the above mixture. After that, NaHCO_3 solution (0.1 M) was dropped into the above system slowly under magnetic stirring in the dark, followed by stirring for another 2 h. The collected solid was washed, and dried at 70 °C overnight. By varying the added amounts of AgNO_3 , NaHCO_3 , and $\text{NH}_3 \cdot \text{H}_2\text{O}$, the as-prepared $\text{Ag}_2\text{CO}_3/\text{Bi}_2\text{MoO}_6$ heterojunctions with various weight ratios (0. 1/1, 0.2/1, 0.3/1 and 0.5/1) were obtained and denoted as ACO/BMO-10, ACO/BMO-20, ACO/BMO-30, and ACO/BMO-50, respectively. For comparison, pure Ag_2CO_3 was prepared by the same method without the addition of Bi_2MoO_6 . A mixture of Ag_2CO_3 and Bi_2MoO_6 , symbolized as mixture, was prepared by simple physical mixing.

Characterization

The microstructure of the samples was observed with a Hitachi S-4800 scanning electron microscope (SEM) and a JEM-2010F transmission electron microscope (TEM). The corresponding chemical compositions were detected by energy-dispersive X-ray (EDX) spectroscopy equipped on the SEM. The crystal structure of catalysts was identified by X-ray diffractometry (XRD, Bruker D8 Advance) with a scanning range of 2θ from 20° to 80°. The UV–vis spectra were recorded using an UV-2600 UV–vis spectrophotometer (Shimadzu). The photoluminescence (PL) emission spectra of the samples were re-

corded on a Hitachi F-7000 spectrophotometer, employing an excitation wavelength of 300 nm.

Photocatalytic test

The photo-degradation of RhB, MO, TC and MB was carried out in a reactor containing 40 mg of sample, and 100 mL of RhB (10 mg·L⁻¹), MO (10 mg·L⁻¹), TC (20 mg·L⁻¹) or MB (10 mg·L⁻¹) under visible-light irradiation. A 300 W xenon lamp equipped with a UV-cutoff filter ($\lambda > 400$ nm) served as the light source. First, the suspension was stirred in the dark for half an hour. During reaction, 2 mL of solution was taken at certain intervals, and centrifuged to obtain the supernatant for UV-vis spectrophotometry measurements. Total organic carbon (TOC) tests were executed by the degradation of RhB (50 mg·L⁻¹, 150 mL) solution with 300 mg of ACO/BMO-30 as the catalyst.

Supporting Information

Supporting Information File 1

Additional experimental data.

[<https://www.beilstein-journals.org/bjnano/content/supplementary/2190-4286-9-214-S1.pdf>]

Acknowledgements

This work has been financially supported by the National Natural Science Foundation of China (51708504, 31501573 and 51602049), the Public Projects of Zhejiang Province (2017C32079 and LGN18E080003), the Science and Technology project of Zhoushan (2017C41006, 2016C41012, 2015C21014, 2015C21013) and National Key Research and Development Program of China (2016YFC0400501/2016YFC0400509).

References

- Kumar, S.; Kumar, A.; Bahuguna, A.; Sharma, V.; Krishnan, V. *Beilstein J. Nanotechnol.* **2017**, *8*, 1571–1600. doi:10.3762/bjnano.8.159
- Hong, Y.; Li, C.; Zhang, G.; Meng, Y.; Yin, B.; Zhao, Y.; Shi, W. *Chem. Eng. J.* **2016**, *299*, 74–84. doi:10.1016/j.cej.2016.04.092
- Wang, F.; Li, Q.; Xu, D. *Adv. Energy Mater.* **2017**, *7*, 1700529. doi:10.1002/aenm.201700529
- Wang, W.; Li, G.; Xia, D.; An, T.; Zhao, H.; Wong, P. K. *Environ. Sci.: Nano* **2017**, *4*, 782–799. doi:10.1039/C7EN00063D
- Bora, L. V.; Mewada, R. K. *Renewable Sustainable Energy Rev.* **2017**, *76*, 1391–1421. doi:10.1016/j.rser.2017.01.130
- Li, S.; Hu, S.; Jiang, W.; Liu, Y.; Liu, Y.; Zhou, Y.; Mo, L.; Liu, J. *Beilstein J. Nanotechnol.* **2018**, *9*, 1308–1316. doi:10.3762/bjnano.9.123
- Adhikari, S. P.; Hood, Z. D.; Wang, H.; Peng, R.; Krall, A.; Li, H.; Chen, V. W.; More, K. L.; Wu, Z.; Geyer, S.; Lachgar, A. *Appl. Catal., B* **2017**, *217*, 448–458. doi:10.1016/j.apcatb.2017.05.092
- Adhikari, S. P.; Hood, Z. D.; More, K. L.; Chen, V. W.; Lachgar, A. *ChemSusChem* **2016**, *9*, 1869–1879. doi:10.1002/cssc.201600424
- Ong, W.-J.; Tan, L.-L.; Ng, Y. H.; Yong, S.-T.; Chai, S.-P. *Chem. Rev.* **2016**, *116*, 7159–7329. doi:10.1021/acs.chemrev.6b00075
- Moniz, S. J. A.; Shevlin, S. A.; Martin, D. J.; Guo, Z.-X.; Tang, J. *Energy Environ. Sci.* **2015**, *8*, 731–759. doi:10.1039/C4EE03271C
- Li, S.; Hu, S.; Jiang, W.; Liu, Y.; Liu, J.; Wang, Z. *J. Colloid Interface Sci.* **2017**, *501*, 156–163. doi:10.1016/j.jcis.2017.04.057
- Chen, C.; Ma, W.; Zhao, J. *Chem. Soc. Rev.* **2010**, *39*, 4206–4219. doi:10.1039/b921692h
- Li, S.; Hu, S.; Xu, K.; Jiang, W.; Liu, Y.; Leng, Z.; Liu, J. *J. Colloid Interface Sci.* **2017**, *504*, 561–569. doi:10.1016/j.jcis.2017.06.018
- Zhang, G.; Lan, Z.-A.; Wang, X. *Angew. Chem., Int. Ed.* **2016**, *55*, 15712–15727. doi:10.1002/anie.201607375
- Wang, Q.; Sun, K.; Lu, Q.; Wei, M.; Yao, L.; Guo, E. *Dyes Pigm.* **2018**, *155*, 194–201. doi:10.1016/j.dyepig.2018.03.048
- Dai, W.; Yu, J.; Xu, H.; Hu, X.; Luo, X.; Yang, L.; Tu, X. *CrystEngComm* **2016**, *18*, 3472–3480. doi:10.1039/c6ce00248j
- Long, J.; Wang, S.; Chang, H.; Zhao, B.; Liu, B.; Zhou, Y.; Wei, W.; Wang, X.; Huang, L.; Huang, W. *Small* **2014**, *10*, 2791–2795. doi:10.1002/sml.201302950
- Guo, C.; Xu, J.; Wang, S.; Li, L.; Zhang, Y.; Li, X. *CrystEngComm* **2012**, *14*, 3602–3608. doi:10.1039/c2ce06757a
- Ma, Y.; Jia, Y.; Wang, L.; Yang, M.; Bi, Y.; Qi, Y. *J. Power Sources* **2016**, *331*, 481–486. doi:10.1016/j.jpowsour.2016.09.084
- Yu, C.; Wu, Z.; Liu, R.; Dionysiou, D. D.; Yang, K.; Wang, C.; Liu, H. *Appl. Catal., B* **2017**, *209*, 1–11. doi:10.1016/j.apcatb.2017.02.057
- Dutta, D. P.; Ballal, A.; Chopade, S.; Kumar, A. *J. Photochem. Photobiol., A* **2017**, *346*, 105–112. doi:10.1016/j.jphotochem.2017.05.044
- Zhang, J. L.; Ma, Z. *J. Taiwan Inst. Chem. Eng.* **2017**, *71*, 156–164. doi:10.1016/j.jtice.2016.11.030
- Meng, Q.; Zhou, Y.; Chen, G.; Hu, Y.; Lv, C.; Qiang, L.; Xing, W. *Chem. Eng. J.* **2018**, *334*, 334–343. doi:10.1016/j.cej.2017.07.134
- Sun, Y.; Wu, J.; Ma, T.; Wang, P.; Cui, C.; Ma, D. *Appl. Surf. Sci.* **2017**, *403*, 141–150. doi:10.1016/j.apsusc.2017.01.130
- Ma, D.; Wu, J.; Gao, M.; Xin, Y.; Sun, Y.; Ma, T. *Chem. Eng. J.* **2017**, *313*, 1567–1576. doi:10.1016/j.cej.2016.11.036
- Liang, J.; Liu, F.; Deng, J.; Li, M.; Tong, M. *Water Res.* **2017**, *123*, 632–641. doi:10.1016/j.watres.2017.06.060
- Zhang, M.; Shao, C.; Mu, J.; Zhang, Z.; Guo, Z.; Zhang, P.; Liu, Y. *CrystEngComm* **2012**, *14*, 605–612. doi:10.1039/C1CE05974B
- Li, S.; Shen, X.; Liu, J.; Zhang, L. *Environ. Sci.: Nano* **2017**, *4*, 1155–1167. doi:10.1039/C6EN00706F
- Li, S.; Hu, S.; Jiang, W.; Liu, Y.; Zhou, Y.; Liu, Y.; Mo, L. *J. Colloid Interface Sci.* **2018**, *521*, 42–49. doi:10.1016/j.jcis.2018.03.033
- Li, S.; Hu, S.; Zhang, J.; Jiang, W.; Liu, J. *J. Colloid Interface Sci.* **2017**, *497*, 93–101. doi:10.1016/j.jcis.2017.02.069
- Li, S.; Hu, S.; Jiang, W.; Zhou, Y.; Liu, J.; Wang, Z. *J. Colloid Interface Sci.* **2018**, *530*, 171–178. doi:10.1016/j.jcis.2018.06.084
- Zhang, J.; Ma, Z. *J. Taiwan Inst. Chem. Eng.* **2018**, *88*, 121–129. doi:10.1016/j.jtice.2018.03.043
- Zhang, J.; Liu, H.; Ma, Z. *J. Mol. Catal. A: Chem.* **2016**, *424*, 37–44. doi:10.1016/j.molcata.2016.08.009
- Jiao, Z.; Zhang, Y.; Yu, H.; Lu, G.; Ye, J.; Bi, Y. *Chem. Commun.* **2013**, *49*, 636–638. doi:10.1039/C2CC37324F

35. Xu, D.; Cheng, B.; Zhang, J.; Wang, W.; Yu, J.; Ho, W. *J. Mater. Chem. A* **2015**, *3*, 20153–20166. doi:10.1039/C5TA05248C
36. Yan, M.; Wu, Y.; Yan, Y.; Yan, X.; Zhu, F.; Hua, Y.; Shi, W. *ACS Sustainable Chem. Eng.* **2016**, *4*, 757–766. doi:10.1021/acssuschemeng.5b00690
37. Bao, J.; Guo, S.; Gao, J.; Hu, T.; Yang, L.; Liu, C.; Peng, J.; Jiang, C. *RSC Adv.* **2015**, *5*, 97195–97204. doi:10.1039/C5RA18938A
38. Zhao, X.; Su, Y.; Qi, X.; Han, X. *ACS Sustainable Chem. Eng.* **2017**, *5*, 6148–6158. doi:10.1021/acssuschemeng.7b01040
39. Li, T.; Hu, X.; Liu, C.; Tang, C.; Wang, X.; Luo, S. *J. Mol. Catal. A: Chem.* **2016**, *425*, 124–135. doi:10.1016/j.molcata.2016.10.001
40. Yu, C.; Wei, L.; Zhou, W.; Dionysiou, D. D.; Zhu, L.; Shu, Q.; Liu, H. *Chemosphere* **2016**, *157*, 250–261. doi:10.1016/j.chemosphere.2016.05.021
41. Liu, Y.; Kong, J.; Yuan, J.; Zhao, W.; Zhu, X.; Sun, C.; Xie, J. *Chem. Eng. J.* **2018**, *331*, 242–254. doi:10.1016/j.cej.2017.08.114
42. Pirhashemi, M.; Habibi-Yangjeh, A. *J. Colloid Interface Sci.* **2016**, *474*, 103–113. doi:10.1016/j.jcis.2016.04.022
43. Li, H.; Liu, J.; Hou, W.; Du, N.; Zhang, R.; Tao, X. *Appl. Catal., B* **2014**, *160–161*, 89–97. doi:10.1016/j.apcatb.2014.05.019
44. Yuan, X.; Jiang, L.; Chen, X.; Leng, L.; Wang, H.; Wu, Z.; Xiong, T.; Liang, J.; Zeng, G. *Environ. Sci.: Nano* **2017**, *4*, 2175–2185. doi:10.1039/C7EN00713B
45. Li, S.; Hu, S.; Jiang, W.; Liu, Y.; Liu, J.; Wang, Z. *Mol. Catal.* **2017**, *435*, 135–143. doi:10.1016/j.mcat.2017.03.027
46. Liu, Y.; Yang, Z.-H.; Song, P.-P.; Xu, R.; Wang, H. *Appl. Surf. Sci.* **2018**, *430*, 561–570. doi:10.1016/j.apsusc.2017.06.231
47. Liu, J.; Li, Y.; Ke, J.; Wang, S.; Wang, L.; Xiao, H. *Appl. Catal., B* **2018**, *224*, 705–714. doi:10.1016/j.apcatb.2017.11.028
48. Li, S.; Hu, S.; Xu, K.; Jiang, W.; Liu, J.; Wang, Z. *Nanomaterials* **2017**, *7*, 22–34. doi:10.3390/nano7010022
49. Feizpoor, S.; Habibi-Yangjeh, A. *J. Colloid Interface Sci.* **2018**, *524*, 325–336. doi:10.1016/j.jcis.2018.03.069
50. Li, S.; Zhang, J.; Hu, S.; Xu, K.; Jiang, W.; Liu, J. *J. Alloys Compd.* **2017**, *695*, 1137–1144. doi:10.1016/j.jallcom.2016.10.240
51. Adhikari, S. P.; Dean, H.; Hood, Z. D.; Peng, R.; More, K. L.; Ivanov, I.; Wu, Z.; Lachgar, A. *RSC Adv.* **2015**, *5*, 91094–91102. doi:10.1039/C5RA13579F
52. Li, S.; Hu, S.; Jiang, W.; Liu, Y.; Liu, Y.; Zhou, Y.; Mo, L.; Liu, J. *Front. Chem. (Lausanne, Switz.)* **2018**, *6*, No. 255. doi:10.3389/fchem.2018.00255
53. Ye, R.; Zhao, J.; Wickemeyer, B. B.; Toste, F. D.; Somorjai, G. A. *Nat. Catal.* **2018**, *1*, 318–325. doi:10.1038/s41929-018-0052-2
54. Zhang, P.; Wang, T.; Chang, X.; Gong, J. *Acc. Chem. Res.* **2016**, *49*, 911–921. doi:10.1021/acs.accounts.6b00036

License and Terms

This is an Open Access article under the terms of the Creative Commons Attribution License (<http://creativecommons.org/licenses/by/4.0>). Please note that the reuse, redistribution and reproduction in particular requires that the authors and source are credited.

The license is subject to the *Beilstein Journal of Nanotechnology* terms and conditions: (<https://www.beilstein-journals.org/bjnano>)

The definitive version of this article is the electronic one which can be found at:
doi:10.3762/bjnano.9.214